# Microelectrode Velocity Effects and Aquatic Eddy Covariance Measurements under Waves

CLARE E. REIMERS, H. TUBA ÖZKAN-HALLER, AND ANDREA T. ALBRIGHT

*College of Earth, Ocean and Atmospheric Sciences, Oregon State University, Corvallis, Oregon*

PETER BERG

*Department of Environmental Sciences, University of Virginia, Charlottesville, Virginia*

(Manuscript received 23 February 2015, in final form 7 December 2015)

ABSTRACT

Interest in validating the eddy covariance (EC) technique under wave-induced flows led to a series of experiments in a 104-m-long large wave flume (LWF) using an acoustic Doppler velocimeter (ADV) and two oxygen microelectrodes (tips ~2 mm apart) mounted on a sturdy tripod. Four additional ADVs positioned within the flume provided comparative near-bed velocity measurements during experiments with irregular waves over a sand bed. These measurements revealed that modifications of local turbulence by the tripod frame were insignificant. However, errors in velocity measurements were at times observed for setups where the microelectrode tips protruded into the ADV's measurement volume. Disparate oxygen microelectrode velocity effects (stirring sensitivities) combined with response time offsets were also identified as problems, adding biases to EC flux derivations. Microelectrode velocity effects were further investigated through modeling designed to mimic the LWF data, and through examination of a 12-h dataset from the Oregon shelf. The modeling showed that under progressive waves, an artificial EC flux, or bias, arises most severely when the velocity sensitivity of the microelectrode is unequal in opposing flow directions or augmented by horizontal currents, and the velocity and oxygen data are not perfectly aligned in time. Sensitivities to wave motions were seen in the oxygen measurements from the Oregon shelf, contributing to an average flux of $+2.7 \pm 0.6$ mmol $m^{-2}$ $day^{-1}$ (SE, $n = 22$) at wave frequencies. Since overall EC fluxes equaled only $-4.1 \pm 1.8$ mmol $m^{-2}$ $day^{-1}$ (SE, $n = 22$), sources of EC biasing coupled to waves cannot be ruled out as potential problems for estimating exact benthic oxygen fluxes under common continental shelf field conditions.

## 1. Introduction

Aquatic eddy covariance (EC), also called eddy correlation, is a method used to derive benthic fluxes under natural flow, light, and biogeochemical conditions. Since introduced by Berg et al. (2003) for studies of benthic oxygen exchange, the limits of the technique and the sensors employed have been tested under increasingly complex conditions, including coastal sites where the local hydrodynamics are dominated by waves and/or variable currents (Kuwae et al. 2006; Holtappels et al. 2013; McCann-Grosvenor et al. 2014; McGinnis et al. 2014). In water depths less than 100 m, surface waves in particular produce distinctive frequency-banded, oscillatory flows that add to the turbulent kinetic energy of currents close to the seabed (Grant and Madsen 1986). Observations show these motions often put fine-grained sediments in suspension and produce rippled sand beds that are permeable, subject to pore fluid advection, and biochemically active (Huettel and Webster 2001; Rusch et al. 2003; Reimers et al. 2004). Thus, coastal environments with persistent wave motions in the benthic boundary layer are expected to show both high and temporally variable uptake rates for dissolved oxygen (Jahnke et al. 2005; Berg and Huettel 2008; Berg et al. 2013).

Interest in testing the reliability of the eddy covariance technique under wave-induced flows and over a sandy bed led here to a series of experiments in a large wave flume (LWF) using a sturdy tripod frame called a benthic oxygen exchange rate (BOXER) lander

*Corresponding author address*: Clare E. Reimers, College of Earth, Ocean and Atmospheric Sciences, Oregon State University, 104 CEOAS Administration Bldg., Corvallis, OR 97331-5503.
E-mail: creimers@coas.oregonstate.edu

DOI: 10.1175/JTECH-D-15-0041.1

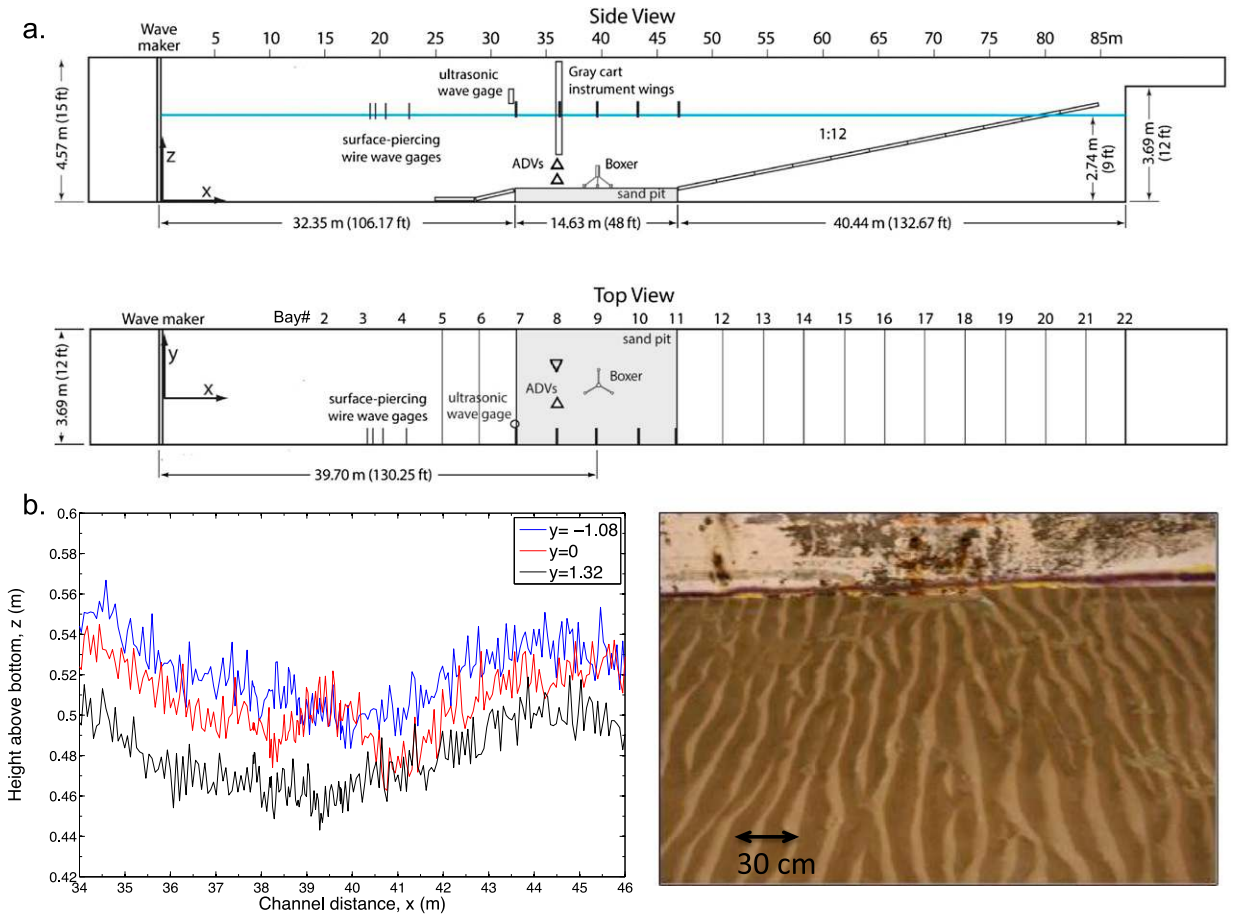


FIG. 1. (a) Schematic drawing of the experimental set up in the O.H. Hinsdale LWF. (b) (left) Example transducer profiles showing bed height variations along and across the sand bed, and (right) image of ripples remaining in the sand after the LWF was drained at the end of experiments.

(Reimers et al. 2012) instrumented with an acoustic Doppler velocimeter (ADV) and oxygen microelectrodes as the principal collocated EC sensors. BOXER was specifically designed to provide a stable platform for autonomous EC measurements in continental shelf environments with high bottom shear stresses and has yielded oxygen fluxes comparable to benthic chambers during studies of the Oregon shelf (Reimers et al. 2012; Fuchsman et al. 2015). Since EC relies on simultaneous measurements of vertical velocity ($w$) and dissolved oxygen concentration ($C$) at positions typically 10–30 cm above a benthic surface, we focused on 1) how the location of the ADV sampling volume, or the presence and orientation of the BOXER frame/sensors may affect time series from within a flume's wave-bottom boundary layer; and 2) how velocity sensitivities of oxygen microelectrodes may add bias to sensor responses and flux extractions. The velocity sensitivities of microelectrodes observed in the LWF also caused us to model the effects of these spurious variations and to look for similar effects within observations from the Oregon shelf where we continue to focus investigations of processes controlling rates of benthic oxygen consumption.

## 2. Experimental conditions, instrumentation, and supporting measurements

### a. *LWF*

The principal laboratory experiments discussed here took place in the O. H. Hinsdale Wave Research Laboratory at Oregon State University in a 2D wave channel that is 104 m long, 3.7 m wide, and 4.6 m deep (Fig. 1). Twenty-two sections or "bays" are marked along the walls to aid the location of instruments. An $xyz$ coordinate system for describing positions in the channel is defined such that $x = 0$ is at the average position of the face of the wave maker when neutrally positioned, $z$ is positive upward, and $z = 0$ is the elevation of the bottom at the location of the wave maker. The coordinate $y$ is

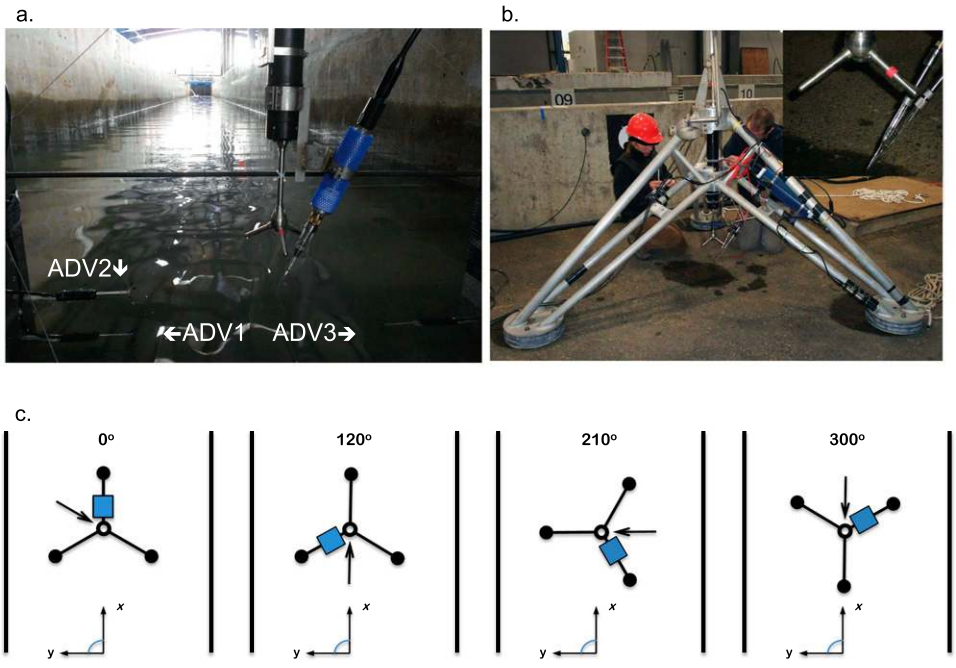


FIG. 2. (a) Image of the four ADVs mounted on wing extensions that were lowered from the flume cart. (b) BOXER frame outside the LWF showing the locations of the controller, optode, and sensors (magnified in inset). (c) Range of BOXER orientations used in the LWF, shown schematically. Blue square and arrow symbolize the controller housing and microelectrode orientation, respectively.

positive to the left when facing in a $+x$ direction and $y = 0$ is at the alongshore centerline of the wave tank (Fig. 1a). Before water was added to the channel, a bed of fine sand (median grain size = 0.22 mm; permeability = 3.7 ($\pm$2.1 SD) $\times$ $10^{-11}$ $m^2$; thickness nominally 0.5 m) was emplaced over the full width of a 14.6-m-long section of the flume starting at $x = 32.35$ m and seeded with labile organic matter by raking 18 kg of Plankton Gold Flake fish food into the entire surface area. Beyond the sand bed the bottom of the flume rose at a 1:12 slope to mimic the presence of a shoreline.

Freshwater was added to the flume 9 days prior to the start of experiments and was allowed to equilibrate to the temperature in the facility (~8°C). The experiments themselves took place over 10 days in March 2012. Waves were run during the setup period to mix the sand bed, form a pattern of cross-channel ripples, and stimulate the onset of oxygen consumption by the bed. To characterize the ripples and assess sand movement, bathymetry surveys of the bed were collected during the setup period and on each experimental day. This procedure involved moving 32 evenly spaced carriage-mounted bottom profiler transducers (SeaTek) down the length of the flume (element 1 surveyed at $y = -1.08$ m and element 32 at $y = 1.32$ m). These surveys showed broadscale variations in bottom elevation over the length and width of the sand bed, as well as small-scale profile changes of 2–3 cm due to the migration of ripples of similar heights (Fig. 1b).

Waves were made with a piston-type hydraulically actuated generator. Wave runs were always programmed to be irregular with significant wave heights ($H_s$) of either 0.3, 0.5, 0.6, or 0.7 m and peak periods ($T_p$) of either 2, 4, or 8 s. Three or four wave runs of 0.33–3-h duration (experimental trials) were run each day.

The LWF was equipped with surface-piercing wire wave gauges and an ultrasonic wave gauge at positions indicated in Fig. 1a. In addition, a cross-channel array of four ADVs was set up on vertical ''wing'' extensions from the cart that was used for transducer surveys (Fig. 2a). This cart straddles the channel and can roll up and down the length on wheels that rest on the channel walls. For each experiment, the cart was locked into position over the sandpit so that the wing-mounted ADVs were at $x = 35.86$ m (Fig. 1a). Three of the ADVs were four-beam 10-MHz Vectrino (Nortek AS) 3D velocity sensors that were positioned so their beams were directed horizontally. Two of these Vectrinos were in parallel orientation sampling at approximately 15 and 30 cm above the sand bed, respectively, and the third Vectrino was opposite the first Vectrino at 15 cm (Fig. 2a). The fourth ADV was a fixed stem, three-beam,

TABLE 1. LWF velocity sensor locations.

| Sensor Name | Placement $x$ (m) | Placement $y$ (m) | Placement $z$ (flume coordinates) (m) |
|---|---|---|---|
| ADV1 (Vectrino DL-7208) | 35.86 | 0.02 | 0.65 |
| ADV2 (Vectrino DL-7248) | 35.86 | 0.02 | 0.80 |
| ADV3 (Vectrino DL-7130) | 35.86 | 0.57 | 0.64 |
| Wing Vector (Head ID VEC 3284) | 35.89 | 0.33 | 0.80 |
| BOXER Vector (Head ID VEC 4868) | 39.7 ± 0.1 | 0 ± 0.1 | 0.65 ± 0.02 (E12); 0.80 ± 0.02 (E5, E8, E10, E11) |

6-MHz Vector (Nortek AS) with standard pressure, temperature, and tilt and roll sensors, mounted vertically and in the center of the channel. Its measurement volume was also set to target a position 30 cm above the bed. This information is summarized in the channel coordinates in Table 1.

### b. *Field case*

To illustrate sensor responses in a natural wave environment, one EC dataset was chosen from a series of BOXER deployments made from the R/V *Oceanus* during cruise OC1307A to the Oregon continental shelf. The site (43°55.89′N, 124°11.74′W) has a mean water depth of 48 m, and EC measurements (as described below) were made on 14 July 2013 starting at 0915 (local time). Over the course of the 12-h deployment, significant wave heights (estimated from near-bottom pressure variations) ranged from 0.5 to 1.2 m with periods of 7.8–8.3 s. These periods matched the dominant periods recorded at an offshore buoy (NDBC station 46229), and the buoy records also document that the dominant wave direction was from the northwest (324°–338°). Bottom photos captured by the BOXER camera showed a sandy seabed marked by bioturbation pits and mounds imprinted on remnant ripples. A CTD cast corresponding to the start of the deployment recorded a bottom water temperature of 7.37°C and salinity of 33.92.

### c. *BOXER and EC sensors*

BOXER is an aluminum tripod that weighs approximately 230 kg in air, is 1.8 m high, and is 2.3 m wide—if measured from the outside of one pod to the outside of another (Fig. 2b). Two circular lead plates are bolted to each pod for ballast, and a rotating camera and strobe assembly may be mounted at its apex (Reimers et al. 2012). Each leg is formed by three aluminum pipes [outer diameters (ODs) of 4.8 or 6.0 cm; Fig. 2b] that rise from the pods to meet two central cylinders (24-cm OD) designed to support a fixed stem Nortek Vector in a vertical orientation. In the present study, the Vector and two oxygen microelectrodes with high-end in situ eddy amplifiers (Unisense AS) were used as the EC sensors, and these were cabled to a commercially available EC controller/logging system (Eddy Correlation System$^2$, Unisense AS) clamped to one of the BOXER's legs (Fig. 2b). Oxygen concentrations and temperature in the water close to the bed were also monitored with 1 or 2 optodes (Aanderaa Instruments AS, model 3835) fixed to the same leg as the controller (Fig. 2b).

BOXER was deployed during all flume experiments so that it was positioned at a location shoreward of the wing ADVs, at $x = 39.7 \pm 0.1$ m and $y = 0 \pm 0.1$ m in the LWF (Fig. 1a). Its Vector was configured for continuous sampling at 64 Hz with a nominal velocity range of either $\pm 0.3$ or $\pm 1.0\,\mathrm{m\,s^{-1}}$. To evaluate possible effects of the frame or its attached equipment on the local turbulence, different orientations with respect to the channel coordinate system were compared (Fig. 2c). The Vector's sampling volume was set to either 15 or 30 cm above the base of the pods—a horizon assumed to equal the average level of the sand–water interface.

In the field case, the deployment was conducted as described by Reimers et al. (2012), the Vector's nominal velocity range was set to $\pm 0.1\,\mathrm{m\,s^{-1}}$, and the Vector's bottom echo function was utilized to access the sampling volume height (equaling 24.5 cm). Two optodes were positioned to sample at 21 and 46 cm above the bed, respectively. They sampled every 10 s and were calibrated prior to the deployment in common seawater solutions. However, to minimize interpretation of a likely small offset between these sensors, we will focus on how the difference between the two sensors changed with time, not the absolute values of the difference.

The microelectrodes used in this study were constructed in our laboratory following the Clark-type design of Revsbech (1989). They were oriented side by side, pointing down at a ~65° angle from horizontal, and the tips were positioned ~0.2 cm outside the Vector sampling volume using a guide fixed to the Vector stem. Gundersen et al. (1998) and Glud et al. (2000) have modeled the geometry of components within the tips of such sensors and present predictive equations for sensor signal strength, 90% response time ($t_{90}$), and stirring sensitivity (defined as the percent change in a sensor's signal strength under rapid

TABLE 2. Properties of microelectrodes from which data are reported. Calibration slopes, response times, and stirring sensitivities were derived from the measurements. As discussed in the text, these properties are not necessarily fixed and especially the stirring sensitivity can depend on the sensor orientation with respect to the flow.

| Sensor | Cathode tip diameter ($\mu$m) | Length of gold plating ($\mu$m) | Cathode to membrane $Z_e$ ($\mu$m) | Membrane length $Z_m$ ($\mu$m) | Tip opening diameter $2r_2$ ($\mu$m) | Calibration slope (mV $\mu$M$^{-1}$) | Response time (s) | Stirring sensitivity* (%) | Expt/ (Channel No.) |
|---|---|---|---|---|---|---|---|---|---|
| 183 | 1.9 | 19 | 1.9 | 7.6 | 2.85 | 5.13 | 0.5 | 1.2 | LWF E11 (C1) |
| 196 | 1.9 | 9.5 | 5.7 | 3.8 | 2.85 | 1.86 (E11) | 0.375 | 0.4 | LWF E11 (C2) |
| | | | | | | 2.02 (E12) | | 0.6 | LWF E12 (C2) |
| 297 | 1.9 | 17.1 | 1.9 | 5.7 | 1.9 | 4.57 | 0.5 | 1.65 | Field case (C1) |

* The asterisk means that it is inferred from measurements in the flume or field.

flow conditions compared to its signal in stagnant water at the same $O_2$ concentration). Using their notation, glass tip openings at the inner and outer membrane surfaces ($2_{r1}$ and $2_{r2}$, respectively), membrane thicknesses ($Z_m$), and the distance of the sensing cathode to the membrane ($Z_e$) were made small to favor rapid response ($t_{90} \leq 0.5$ s) as required to prevent signal loss in EC (Lorrai et al. 2010; Donis et al. 2015; Berg et al. 2016) (Table 2). As an undesired trade-off, stirring sensitivities were <1%–2%. Such effects are nonlinear and often asymmetric with respect to flow speed and direction, and are caused by alterations of a spherical boundary layer surrounding the tip (Gust et al. 1987; Holtappels et al. 2015). An $O_2$ gradient across the boundary layer is set up by the internal consumption of $O_2$ at the cathode. A steeper gradient under rapid flow will produce a higher microelectrode signal (and faster response time) even though the ambient $O_2$ concentration is unchanged. We will refer to this sensitivity to flow variations as a microelectrode's velocity effect (VE), and we will subsequently model this nonideal response to assess its impacts on EC fluxes under waves.

Microelectrode time series to be reported were recorded on BOXER. Microelectrode time series collocated with the wing Vector velocities in the LWF (Fig. 2a) were intended for comparison but were consistently contaminated by an unidentified source of oscillatory noise at ~0.1 Hz. At the wing, an autozeroing picoamplifier (an earlier product of Unisense and originally designed at the Max Planck Institute for Microbiology; see also Berg et al. 2009) was used to capture the microelectrode signal variations. Although battery powered through the Vector, this amplifier was apparently sensitive to an unknown noise source in the LWF facility.

### *d. Incubations and $O_2$ microprofiles from the LWF*

Core incubations were used to obtain estimates of oxygen consumption by the sand bed in the LWF that could be compared with EC fluxes. Three sediment cores [tube inner diameter (ID) = 9.4 cm; length = 30 cm; length of sand columns = 21.6–24.4 cm] were collected by scuba divers from the area of the sand bed just shoreward of the BOXER position. These were carefully sealed underwater with tops having double O-ring seals and a centered magnetic stir bar rotating in the overlying water under the control of an outer magnet turned by an electric motor. Incubations occurred over a period of 3 h with the cores held in the dark in a bucket of water at 8°C. Oxygen was measured at discrete time points separated by 8–38 min using a needle-type Fibox Optical Sensor (PreSens Precision Sensing GmbH) introduced into the overlying water volume through a sampling port in each lid. From a linear fit to the rate of change of the dissolved oxygen, and the volume and area of overlying water in each core tube, total oxygen consumption rates were calculated. These equated to $-10.4 \pm 3.0$ (SD, $n = 3$) mmol m$^{-2}$ day$^{-1}$.

Oxygen microprofiles across the sediment–water interface were also determined using microelectrodes supported by a microprofiling instrument mounted on a small tripod frame that was originally built for remotely operated vehicle deployments. The instrument was lowered into the LWF with a rope at approximately $x = 35$ m on the first day of experiments before any waves were run, and on a few later days while waves were being generated. The profiling resolution was 0.25 mm, and diffusive oxygen uptake estimates equal to $-11.5 \pm 1.5$ mmol m$^{-2}$ day$^{-1}$ (SD, $n = 2$) were determined from the no-wave-state concentration gradients in the first 1.0 mm beneath the sediment–water interface using Fick's law of diffusion (Fick 1855; Glud 2008). The diffusion coefficient for $O_2$ was set to equal $1.42 \times 10^{-5}$ cm s$^{-1}$ (Boudreau 1997), and the porosity of the sand was assumed = 0.6. There was no evidence of any living algal community in the LWF that could support oxygen production within the bed or water column.

## 3. EC data collection and treatments

### a. LWF experiments

In total, 15 experiments were conducted in the LWF involving 34 continuous wave runs lasting from 20 to 180 min. Here, attention is focused primarily upon experiments run with $H_s = 0.3$ m or 0.5 m, and a peak period $T_p = 4$ s. Time series data collected at 64 Hz using the Unisense EC system and the separate ADVs were aligned and examined in 30-min intervals. Seeding particles added to the flume water helped to ensure that ADV records showed high beam correlations (generally $> 95\%$). The oxygen microelectrode outputs were calibrated using points set by a zero-concentration reading recorded in a chilled anoxic 10% solution of 1-M sodium ascorbate and a 0.5-M NaOH solution before deployment, and a 40-s average of readings referenced to optode measurements made in situ at the time series midpoint. Velocity and oxygen measurements were then despiked using the method developed by Goring and Nikora (2002), and after recording the number of outliers (in all cases $< 3\%$), all removed points were replaced using a cubic spline interpolation. After despiking, the data frequency was reduced to 8 Hz by averaging every eight points.

All 30-min-long 8-Hz ADV data records were corrected for alignment variations by rotating the coordinate system first around the $z$ axis and then around the $y$ axis to maximize the horizontal velocity in the $+x$ direction, $u$, and to minimize the standard deviation of the vertical wave velocity (Reimers et al. 2012). This procedure recognized changes in the BOXER's orientation and tilt, and it confirmed that each wing ADV was mounted with its $x$ axis aligned with the $x$ direction of the flume to within 3°. Symmetric plots of $w'$ versus $u'$ and Reynolds stress ($\overline{u'w'}$) calculations made after these rotations also verified that vertical velocities were not inadvertently contaminated with horizontal motions. Thus, we assume very minimal "apparent turbulence and wave bias" due to leveling errors as described in Shaw and Trowbridge (2001).

### b. Field experiment

Field data were also collected continuously at 64 Hz, despiked, reduced to 8 Hz, and rotated as mentioned above. Oxygen microelectrode signals were calibrated by cross-referencing to optode readings at 10 discrete time points and performing a single linear regression. The intercept of this regression was checked to make sure it nearly matched zero-concentration readings recorded in a chilled anoxic 10% solution of 1-M sodium ascorbate and a 0.5-M NaOH solution before and after deployment.

### c. Eddy fluxes, spectral analyses, and models

Linear detrending was applied to 8-Hz data to calculate fluctuating portions of each velocity component $u'$, $v'$, $w'$, and of the oxygen concentration $C'$. This detrending method was chosen so to preserve low-frequency variations and was applied to both flume and field time series, usually in 30-min segments after rotating the velocities. In addition, selected 2-min segments were analyzed to illustrate wave velocity effects. The averaged product $\overline{w'C'}$ was used to calculate eddy fluxes of dissolved oxygen both without and with shifting the oxygen time series to compensate for inherent sensor response time differences. These response lags of the oxygen microelectrodes were evaluated with cross-correlation routines run in MATLAB (MathWorks), applying the xcorr function to identify time shifts giving minimum and maximum correlations between $u$ (as well as other velocity parameters) and $C'$, using 2-min time series. As will be shown here, a strong correlation between $u$ and $C'$ can stem from asymmetric velocity effects under progressive waves, but such correlations are also expected when there is a near-bed $O_2$ gradient that is displaced in phase with each wave's fluid velocity in the direction of propagation [a phenomenon potentially producing large biases in EC flux extractions, as explored in detail by Berg et al. (2015)]. Spatial separation of sensors can also be a factor affecting time series correlations when water parcels in motion encounter one sensor before reaching the other (Donis et al. 2015). However, under oscillatory flow any effect of positioning would produce time shifts relative to the velocity time series that are also oscillating (i.e., both leading and lagging). Thus, spatial offsets needed to be kept small in these experiments (~0.2 cm as described above) to minimize instantaneous response differences during each wave cycle.

Fluctuations of velocities observed in the LWF were further studied by computing their bandpassed standard deviations in four frequency ranges meant to represent signals that were predominantly 1) noise ($f \geq 1$ Hz), 2) turbulence ($1\text{ Hz} \geq f \geq 0.35$ Hz), 3) wave motions ($0.35\text{ Hz} \geq f \geq 0.15$ Hz), or 4) seiching within the LWF ($0.15\text{ Hz} \geq f$). These ranges were deduced from examinations of energy density spectra of $w'$ (Shaw and Trowbridge 2001). Cumulative cospectra of $C'$ and $w'$ were calculated over the frequency range of $4\text{ Hz} \geq f \geq 0.0005$ Hz to illustrate the variation of flux contributions with eddy frequency. Models to examine the effects of different combinations of wave parameters and velocity effect signals in $C'$ were constructed in MATLAB.

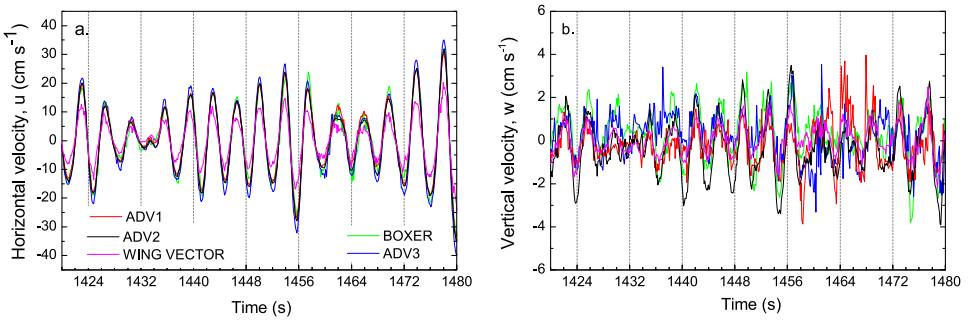


FIG. 3. Example of comparative velocity time series—(a) $u$ and (b) $w$—for irregular waves targeting $H_s$ = 0.3 m, $T_p$ = 4 s in the LWF. Line colors identify the same ADVs in both (a) and (b).

## 4. Results

### a. Velocity measurements under waves

Velocity measurements made in the LWF were analyzed first to determine if there were any significant differences in velocity component fluctuations sensed by the ADVs mounted on the wing extensions and on BOXER. Such differences especially in $w'$ could be reflected in eddy flux determinations and might be attributable to sensor type (Vectrino vs Vector), ADV orientation (horizontal vs vertical), $xyz$ position in the LWF, and/or modification of the local hydrodynamics by the BOXER frame. The problem was approached by examining results within and comparing results between four nearly identical wave runs conducted as trials within four experiments on different days (E2, E5, E8, E10). In each trial the same sequence of irregular waves was generated to target a sea state with $H_s$ = 0.3 m and $T_p$ = 4 s. All five ADVs collected data simultaneously in only one of the experiments (E5) (due to problems with power supplies). However, by pooling the similar runs, we were able to intercompare all the ADVs repeatedly.

A first observation is that all of the rotated $u$ and $w$ time series displayed the strong influence of progressive wave motions (Fig. 3). However, the relative magnitudes of wave variations compared to turbulent variations were greater in $u$ than in $w$, and variations in $w$ appeared more location (or sensor) dependent (Fig. 3). The major factors distinguishing position were that ADV1 and ADV2 were aligned in $x$ and $y$ positions; the BOXER and wing Vectors were centrally located in the $y$ direction; BOXER was uniquely down channel; and ADV2, wing, and BOXER (E5, E8, E10) sampling volumes were ~15 cm higher above the bottom than ADV1 and ADV3 (Table 1).

When evaluating velocity variations by frequency band for the four similar experimental runs, Fig. 4 shows that not all sensors measured equivalent motions. Notably ADV3 (one of the Vectrinos at 15 cm above bottom) reported greater $u'$ variations, and the two Vectors did not give consistent $u'$ or $w'$ variations at wave frequencies between similar trials. Furthermore, noise levels in $u'$ and $v'$ show up as much higher for the Vectors (note the scale difference across the panels in Fig. 4a). The influence of sampling height is best evaluated by comparing ADV2 (~30 cm above sediment) to ADV1 and ADV3 (~15 cm above sediment). Predictably, there is a stronger vertical wave component at the higher sampling position, while the amount of turbulence detected (assessed from std$w'$ 1 Hz $\geq f \geq$ 0.35 Hz) is similar between the three Vectrinos. This implies that both sampling positions were above the near-bed zone, where ripple–flow interactions increase the level of turbulence (Doering and Baryla 2002).

Figure 4a also shows no indication that $w'$ variations at frequencies dominated by high-frequency turbulence were enhanced by flow interactions with the BOXER's frame or mounted equipment. To examine this further, we analyzed variations in velocity components (using the same frequency bands) with BOXER in four different orientations (Fig. 2c) under 30 min of irregular waves where $H_s$ = 0.5 m and $T_s$ = 4 s (E12) (Fig. 4b). As shown diagrammatically in Fig. 2c, the least frame interference was expected when the tripod was positioned without a leg or microelectrode amplifiers and mounts directly in the wave path (orientation = 210°). The outcome (Fig. 4b) shows all determinations of std$w'_{\text{turb}}$ were equivalent to within a 95% confidence level of the mean, but the lowest std$w'_{\text{turb}}$ was at the 210° angle. This is consistent with some small-scale turbulence being added by the frame while also indicating these effects are relatively minor compared to the background turbulence under waves.

### b. Oxygen microelectrode measurements and fluxes

In this study, one effect that was found to have a significant impact is the velocity effect of $O_2$ microelectrodes under short period waves. Figure 5 shows a 2-min time series from paired $O_2$ microelectrodes on BOXER

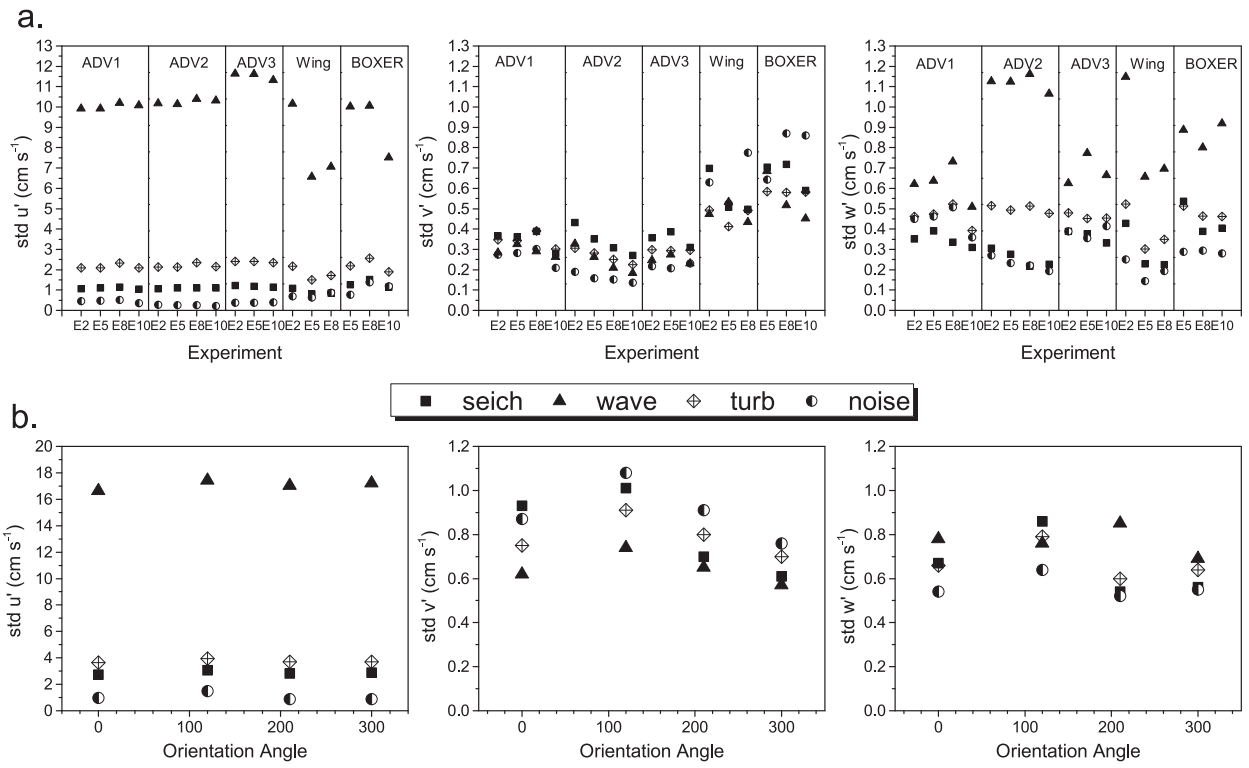


FIG. 4. (a) Measured standard deviations in velocity time series by frequency bands associated predominantly with noise, turbulence, waves, and seiching during LWF experiments with $H_s = 0.3$ m and $T_p = 4$ s. (b) Standard deviations in velocity time series by frequency bands, in four BOXER orientations depicted in Fig. 2c, from irregular wave runs with $H_s = 0.5$ m and $T_p = 4$ s.

in the 300° orientation (Fig. 2c) determined under irregular waves during LWF E11, where $H_s = 0.5$ m and $T_s = 4$ s. Because of variable velocity effects, true oxygen variations are difficult to identify and the two sensors display unequal apparent changes in oxygen concentration that rise and fall roughly every half-wave period. In this example, which was typical for the flume experiments, the amplitude of the variations for the C1 sensor (183, Table 2) rises to ~5 $\mu$M above the minimum signal and for C2 (196; Table 2) amplitudes rise by ~2 $\mu$M. The unequal variations in the $O_2$ time series when separated by linear detrending over the 2-min series and combined with the variations in $w$ yield very different $O_2$ eddy flux estimates (equivalent to $-1130$ and $-162$ mmol m$^{-2}$ day$^{-1}$ for C1 and C2, respectively). Because the same velocity data were used, this is a clear indication of one or more $O_2$ sensor problems biasing the outcome.

To decipher the problem(s), the detrended $O_2$ data from just three wave periods (corresponding to 72.13–84.13 s in Fig. 5) are plotted in relation to the dominant velocity component, $u$ in Fig. 6a. This helps illustrate that the velocity dependency for C1 has a striking hysteresis and is unequal with respect to the direction of $u$ (more pronounced when flow is directed toward the microelectrode tip). These velocity effects are smaller by ~67% for C2. Cross-correlation analyses between $u$ and $C'$ for the entire 2-min series yield maximum correlation coefficients when C1 and C2 are shifted 0.5 and 0.375 s, respectively. Figure 6b shows that when time shifted, the data from Fig. 6a collapse to relatively consistent nonlinear but directionally dependent relationships with velocity. Each wave cycle has some variation, but this is presumably because velocity effects and the response lags of these effects do vary, and because true oxygen signal variations arising from parcels of water with slightly different $O_2$ concentrations are also within these data.

Figure 6c shows how varying the time lag correction over half of one wave period (2 s) produces a numeric range of derived eddy fluxes, which is very broad for the sensor with the larger velocity effect (C1). Fluxes at the correlation-based and presumed best time lag adjustments of 0.5 and 0.375 s for C1 and C2 are equivalent to 187 and 47.4 mmol m$^{-2}$ day$^{-1}$, respectively (Fig. 6c). Covariance at wave frequencies drives the sign of these fluxes, and Fig. 6d illustrates this dependence through cumulative cospectra based on a full 30-min segment of E11 (after time shifts of the $O_2$ series). The cumulative cospectra show that positive flux contributions accumulate sharply at twice the dominant wave frequency (~0.5 Hz) in

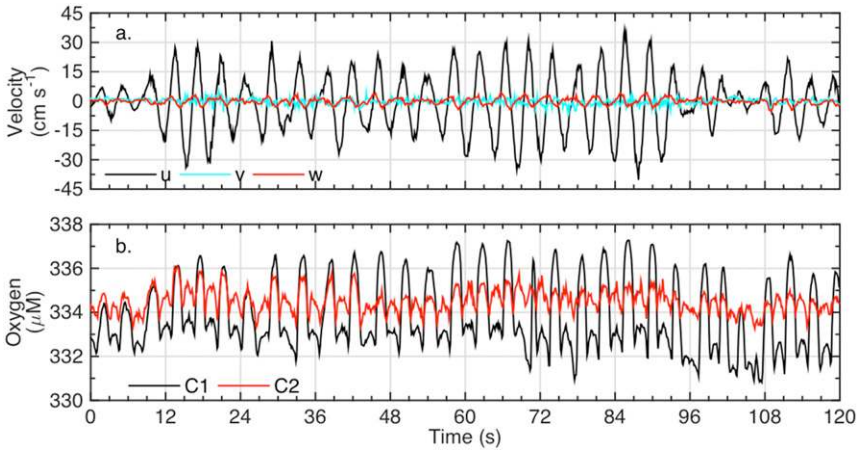


FIG. 5. Segment of an 8-Hz time series from BOXER showing (a) rotated velocities (cm $s^{-1}$) and (b) two $O_2$ microelectrode records ($\mu$M) measured 30 cm above the bed during LWF E11 ($H_s$ = 0.5 m and $T_p$ = 4 s).

both records and then increase again at the dominant wave frequency (0.25 Hz). Only between 0.2 and 0.02 Hz are there smaller negative contributions to the fluxes. Using these 30 min of data, the C1 record predicts a benthic oxygen flux equal to 356 mmol $m^{-2}$ $day^{-1}$ and C2 yields 161 mmol $m^{-2}$ $day^{-1}$.

The independent core incubation or microprofile estimates of the oxygen consumption rate supported by the flume's sand bed equaled approximately −11 mmol $m^{-2}$ $day^{-1}$ (section 2d). Although real differences between this flux and the eddy fluxes might arise from nonsteady-state conditions in the flume—for example, due to the intermittent wave pumping—the lack of agreement between the two simultaneous EC microelectrode records, especially at the wave frequencies, points to a very significant problem primarily caused by the velocity sensitivity of $O_2$ microelectrodes. Below, we show through nonlinear curve fitting that we can largely duplicate the velocity effects and then model how these biases may combine with wave motions to generate false fluxes. We will use related approaches to establish whether eddy fluxes measured in the field are similarly affected.

### c. *Modeling microelectrode velocity effects*

The velocity effects seen in Figs. 5 and 6 suggest the apparent $O_2$ concentration time series under changing velocities, $C(t)$, may be approximated after response time correction by a function such as

$$C(t) = C_{v0b}(t) + (\overline{C}_{vmaxb} - \overline{C}_{v0b})\tanh(\alpha|u(t)|), \quad (1)$$

where $|u(t)|$ represents the magnitude of the horizontal velocity vector directed at or away from the sensor, $C_{v0b}(t)$ represents a baseline oxygen concentration time series with no velocity effect, $\overline{C}_{v0b}$ is the mean of this baseline, and $\overline{C}_{vmaxb}$ is the mean of the same baseline with the addition of the maximum observable velocity sensitivity that may be directionally dependent [i.e., $\overline{C}_{vmaxb}$ for $u(t) \geq 0$ may be different from $u(t) < 0$]. The coefficient $\alpha$ parameterizes how sharply signals increase toward $\overline{C}_{vmaxb}$, and it too may be directionally dependent. In the common terminology introduced earlier, $(\overline{C}_{vmaxb} - \overline{C}_{v0b}/\overline{C}_{v0b})100$ is the stirring sensitivity (%). For more universal cases of nonchannelized flow, such as that which occurs in most field situations, $|u(t)|$ may be replaced by the magnitude of the measured three-dimensional velocity vector at each time point $|U(t)|$ and directionality determined by the sign of $u$ after rotation to orient the greatest flow in the $x$ direction. Accordingly, in following model treatments we define the directional resultant velocity as

$$U(t) = \text{sign}(u)\sqrt{(u^2 + v^2 + w^2)}. \quad (2)$$

Simple rearrangement of Eq. (1) followed by a combination of terms when using the resultant velocity gives

$$C(t) - C_{v0b}(t) = \Delta C_{VE}(t) = \begin{cases} \Delta C_{max+}\tanh(\alpha_+|U(t)|); & \text{for} \quad u(t) \geq 0 \\ \Delta C_{max-}\tanh(\alpha_-|U(t)|); & \text{for} \quad u(t) < 0 \end{cases}. \quad (3)$$

In this expression $\Delta C_{VE}(t)$ represents the false variation in the oxygen signal caused by the effects of time-varying velocity. We have applied a nonlinear curve-fitting software tool (Origin) to parameterize this model with the data from Fig. 5 after approximating $C_{v0b}(t)$ with results of a bandpass filter isolating signals with

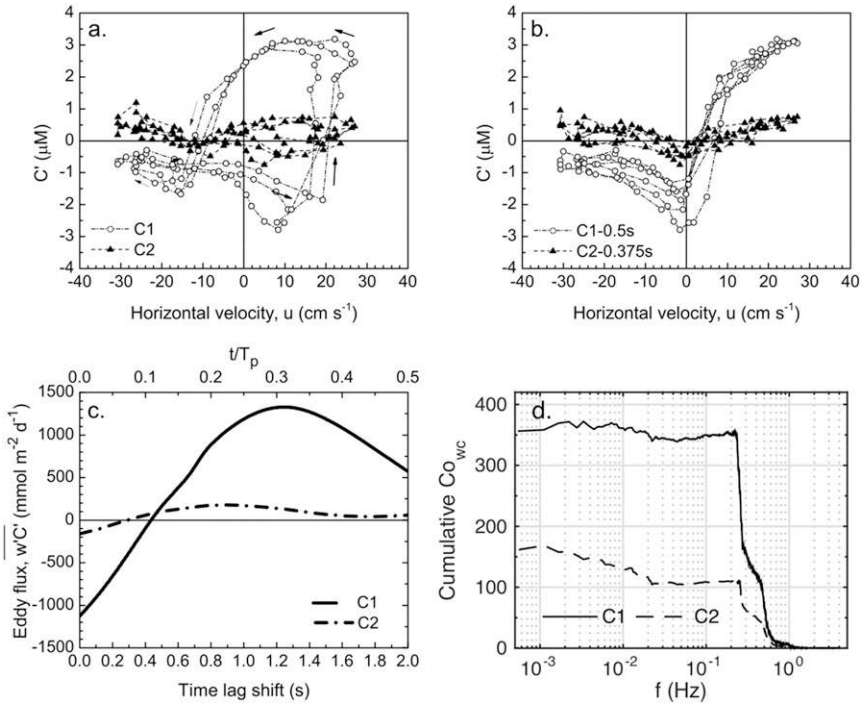


FIG. 6. (a) Data from three E11 wave cycles showing apparent $O_2$ concentration variations vs the dominant horizontal velocity component $u$. Arrows depict the progression of C1 data through one wave. (b) As in (a), but after applying a 0.5-s time lag correction to C1 and a 0.375-s correction to C2. (c) Eddy fluxes derived from the 2-min time series of E11 as a function of time lag shift and $O_2$ record. (d) Cumulative cospectra (mmol $m^{-2}$ $day^{-1}$) of $C'$ and $w'$ derived from a 30-min time series during E11 after time lag shifts of 0.5 s and 0.375 s for C1 and C2, respectively.

frequencies $< 0.05$ Hz within the 2 min of measurements. Accordingly, we found for C1

$$\Delta C_{\mathrm{VE}}(t) = \begin{cases} 4.00\tanh[0.097|U(t)|]; & \text{for} \quad u(t) \geq 0 \\ 0.72\tanh[0.066|U(t)|]; & \text{for} \quad u(t) < 0 \end{cases}$$

and for C2

$$\Delta C_{\mathrm{VE}}(t) = \begin{cases} 1.30\tanh[0.102|U(t)|]; & \text{for} \quad u(t) \geq 0 \\ 0.88\tanh[0.066|U(t)|]; & \text{for} \quad u(t) < 0 \end{cases}.$$

Figure 7a compares curves from these model fits to $\Delta C_{\mathrm{VE}}(t)$ values separated from the measurements. An alternative velocity effect model presented by Holtappels et al. (2015) and Gust et al. (1987) can be fit to measurements similarly (as we will show with later field data), but because it relies on predetermination or fitting of four parameters ($C_\infty$, $S_{\mathrm{sen}}$, $B$, $n$) versus the two in Eq. (3), we prefer the "tanh model."

The reproducibility of a given microelectrode's velocity response and its dependence on orientation with respect to flow was assessed by fitting a second 2-min segment of data collected with the same C2 microelectrode on a different day at a new orientation (i.e., BOXER in its 120° orientation) (Fig. 7b). The model fits to the data in Fig. 7b gave

$$\Delta C_{\mathrm{VE}}(t) = \begin{cases} 1.87\tanh[0.068|U(t)|]; & \text{for} \quad u(t) \geq 0 \\ 2.04\tanh[0.058|U(t)|]; & \text{for} \quad u(t) < 0. \end{cases}$$

Thus, the velocity effect appeared to be larger on the second day, and the greater sensitivity to flow directed toward the sensor tip is seen in the reversal of the asymmetry patterns. In other words, in Fig. 7a velocity effects on average are greater when $u$ is positive, and in Fig. 7b velocity effects are greater when $u$ is negative (although the directional dependency is relatively small for this sensor). The microelectrode properties that are suspected to influence the directional dependency of the velocity effect are 1) how flush the membrane is with respect to the glass at the tip and 2) the distance from the membrane to the cathode (Table 2).

Figure 8 shows that our velocity effect model can explain most of the signal variation seen in short segments

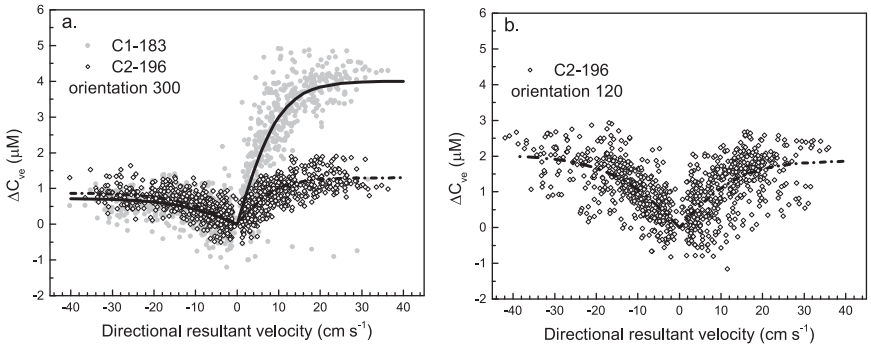


FIG. 7. Velocity effect model fits to microelectrode measurements from 2-min time series during (a) E11 and (b) E12 after time lag correction. The orientation of BOXER during E11 pointed the microelectrodes into $+u$. During E12 one of the same sensors was used, but the orientation was reversed to point into $-u$.

of flume data, suggesting that the $C(t) - \Delta C_{VE}(t)$ series should ideally represent true oxygen variations. However, eddy fluxes derived using these "velocity effect corrected" oxygen series from the 2-min segment of E11 still do not agree, equaling $+63\,\mathrm{mmol\,m^{-2}\,day^{-1}}$ for C1 and $+1.8\,\mathrm{mmol\,m^{-2}\,day^{-1}}$ for C2. The discrepancy is greater when using corrected oxygen series from the 30-min segment of E11. We suspect the issues are that oxygen microelectrode velocity effects have more variability than accounted for by our simple and single tanh model fits, and that variable response times are not accounted for with uniform time shifts. Therefore, we must conclude that under conditions of low natural fluxes and energetic waves as created in the LWF, the oxygen microelectrode time series cannot be simply corrected for velocity effects to derive accurate eddy fluxes.

### d. *Velocity effects with model waves*

To further understand how velocity effects may combine uniquely with progressive wave motions to produce false fluxes and which parameters control the sign and magnitude of these biases, we created a variety of sensor velocity effect, wave, and current model scenarios, and then united them in different combinations to evaluate the relative impacts of assumptions and parameters. The cases and parameter variations are listed in Table 3, and Fig. 9 graphically illustrates two of the model outcomes (cases 4 and 18). From these analyses it is evident that when time series are aligned perfectly, a false flux should not result from any velocity effect (even an asymmetric one similar to C1; Fig. 7a) that is responsive to either $u$ or both $u$ and $w$ velocity components (i.e., cases 1, 4, 6, and 10). This is because the dominant microelectrode response is always out of phase with $w$, so cumulative effects return to zero with each new wave cycle (Fig. 9a).

The introduction of a small offset in the alignment of oxygen and velocity time series, however, can create a sizable false flux from the velocity effect signal when there is a persistent horizontal current (e.g., cases 3 and 9) and/or when the microelectrode velocity effect is asymmetric (e.g., cases 5, and 11–19). The sign of the false flux is dictated by the directional dependence of the velocity effect, which in turn depends on the sensor's orientation with respect to the flow field (e.g., case 11 vs case 12), and by whether $C'$ leads or lags the velocity series (as might be caused by an inaccurate time lag correction). Berg et al. (2015) show that a significant time lag bias can similarly be created under waves when a real oxygen signal (not influenced by velocity effects) is incorrectly aligned with the vertical velocity in time.

The length of the time series offset relative to the wave period is also important, such that a 0.125-s offset in time series alignment produces twice the false flux under 4-s waves compared to 8-s waves (case 11 vs case 15). The presence of a modest steady background current ($5\,\mathrm{cm\,s^{-1}}$) does not greatly alter the consequences of an asymmetric velocity effect (case 15 vs case 16), but

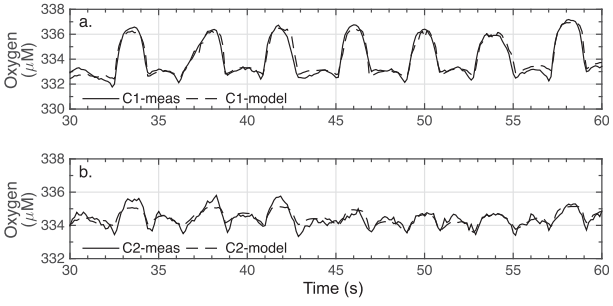


FIG. 8. Comparisons between measured and modeled oxygen concentration time series for a 30-s segment of the data from Fig. 5.

TABLE 3. Summary of model scenarios and their impacts on eddy fluxes derived using linear detrending of 30-min time series of ideal wave velocities. No turbulent variations were included in the velocity series, and the Reynolds stress $\overline{u'w'} \cong 0$ in each case.

| Case ID and illustrative condition(s) | VE formulation | $T_p$ (s) | Wave orbital velocities (cm s$^{-1}$) | Horizontal current velocity (cm s$^{-1}$) | Vertical eddy flux (mmol m$^{-2}$ day$^{-1}$) |
|---|---|---|---|---|---|
| 1. Symmetric VE responsive to horizontal flow only under ideal regular intermediate water waves, no horizontal current | $\Delta C(t) = 4.0\tanh[0.1\lvert u(t)\rvert]$ | 4 | $u = 40\cos\left(-\frac{2\pi}{T_p}t\right)$; $w = 3\sin\left(-\frac{2\pi}{T_p}t\right)$ | 0 | ~0 |
| 2. As in 1, but with a time lag adjustment error of 0.125 s in the oxygen record | $\Delta C(t) = 4.0\tanh[0.1\lvert u(t-0.125)\rvert]$ | 4 | Same as above | 0 | ~0 |
| 3. As in 2, but with steady horizontal current | $\Delta C(t) = 4.0\tanh[0.1\lvert u(t-0.125)\rvert]$ | 4 | Same as above | +5 | −31 (+31 if current direction shifted 180°) |
| 4. Asymmetric VE responsive to horizontal flow only under ideal regular intermediate water waves, no current | $\Delta C(t) = 4.0\tanh[0.1\lvert u(t)\rvert]$; $u \geq 0$<br>$\Delta C(t) = 0.7\tanh[0.07\lvert u(t)\rvert]$; $u < 0$ | 4 | Same as above | 0 | ~0 |
| 5. As in 4, but with a time lag adjustment error of 0.125 s in the oxygen record | $\Delta C(t) = 4.0\tanh[0.1\lvert u(t-0.125)\rvert]$; $u \geq 0$<br>$\Delta C(t) = 0.7\tanh[0.07\lvert u(t-0.125)\rvert]$; $u < 0$ | 4 | Same as above | 0 | −520 (+520 if time lag error = +0.125 s) |
| 6. Symmetric VE responsive to all flow components under ideal regular intermediate water waves, no current | $\Delta C(t) = 4.0\tanh[0.1\lvert U(t)\rvert]$ | 4 | Same as above | 0 | ~0 |
| 7. As in 6, but with a time lag adjustment error of 0.125 s in the oxygen record | $\Delta C(t) = 4.0\tanh[0.1\lvert U(t-0.125)\rvert]$ | 4 | Same as above | 0 | ~0 |
| 8. As in 7, but with greater time lag offset (0.5 s) | $\Delta C(t) = 4.0\tanh[0.1\lvert U(t-0.5)\rvert]$ | 4 | Same as above | 0 | 0.1 |
| 9. As in 8, but with steady horizontal current | $\Delta C(t) = 4.0\tanh[0.1\lvert U(t-0.5)\rvert]$ | 4 | Same as above | +5 | −97 (+97 if current direction shifted 180°) |
| 10. Asymmetric VE responsive to all flow components under ideal regular intermediate water waves, no current | $\Delta C(t) = 4.0\tanh[0.1\lvert U(t)\rvert]$; $u \geq 0$<br>$\Delta C(t) = 0.7\tanh[0.07\lvert U(t)\rvert]$; $u < 0$ | 4 | Same as above | 0 | ~0 |
| 11. As in 10, but with a time lag adjustment error of 0.125 s | $\Delta C(t) = 4.0\tanh[0.1\lvert U(t-0.125)\rvert]$; $u \geq 0$<br>$\Delta C(t) = 0.7\tanh[0.07\lvert U(t-0.125)\rvert]$; $u < 0$ | 4 | Same as above | 0 | −521 (+521 if time lag error = +0.125 s) |
| 12. As in 11, but with directional dependence of VE reversed | $\Delta C(t) = 0.7\tanh[0.07\lvert U(t-0.125)\rvert]$; $u \geq 0$<br>$\Delta C(t) = 4.0\tanh[0.1\lvert U(t-0.125)\rvert]$; $u < 0$ | 4 | Same as above | 0 | +521 (−521 if time lag error = +0.125 s) |
| 13. Asymmetric VE responsive to all flow components with a time lag error of 0.125, smaller directional dependence than in 11 | $\Delta C(t) = 4.0\tanh[0.1\lvert U(t-0.125)\rvert]$; $u \geq 0$<br>$\Delta C(t) = 2.0\tanh[0.07\lvert U(t-0.125)\rvert]$; $u < 0$ | 4 | Same as above | 0 | −324 (324 if time lag error = +0.125 s) |
| 14. Asymmetric VE responsive to all flow components with a time lag error of 0.125, smaller velocity sensitivity | $\Delta C(t) = 2.0\tanh[0.1\lvert U(t-0.125)\rvert]$; $u \geq 0$<br>$\Delta C(t) = 0.35\tanh[0.07\lvert U(t-0.125)\rvert]$; $u < 0$ | 4 | Same as above | 0 | −261 (+261 if time lag error = +0.125 s) |
| 15. As in 11, but with the wave period doubled in duration | $\Delta C(t) = 4.0\tanh[0.1\lvert U(t-0.125)\rvert]$; $u \geq 0$<br>$\Delta C(t) = 0.7\tanh[0.07\lvert U(t-0.125)\rvert]$; $u < 0$ | 8 | Same as above | 0 | −262 |

TABLE 3. (*Continued*)

| Case ID and illustrative condition(s) | VE formulation | $T_p$ (s) | Wave orbital velocities (cm s$^{-1}$) | Horizontal current velocity (cm s$^{-1}$) | Vertical eddy flux (mmol m$^{-2}$ day$^{-1}$) |
|---|---|---|---|---|---|
| 16. As in 15, but with added steady horizontal current | $\Delta C(t) = 4.0\tanh[0.1\lvert U(t-0.125)\rvert]$; $u \geq 0$<br>$\Delta C(t) = 0.7\tanh[0.07\lvert U(t-0.125)\rvert]$; $u < 0$ | 8 | Same as above | +5 | −268 (−251 if current direction shifted 180°) |
| 17. As in 15, but with reduced $w$ (as when close to the seafloor) | $\Delta C(t) = 4.0\tanh[0.1\lvert U(t-0.125)\rvert]$; $u \geq 0$<br>$\Delta C(t) = 0.7\tanh[0.07\lvert U(t-0.125)\rvert]$; $u < 0$ | 8 | $u = 40\cos\left(-\frac{2\pi}{T_p}t\right)$;<br>$w = 0.5\sin\left(-\frac{2\pi}{T_p}t\right)$ | 0 | −44 |
| 18. Asymmetric VE responsive to all flow components with a time lag error of 0.125 s and irregular waves, no current | $\Delta C(t) = 4.0\tanh[0.1\lvert U(t-0.125)\rvert]$; $u \geq 0$<br>$\Delta C(t) = 0.7\tanh[0.07\lvert U(t-0.125)\rvert]$; $u < 0$ | ~4 | Irregular intermediate water waves based on LWF E11 near-bottom pressure time series (see text) | 0 | −76 (+76 if time lag error = +0.125 s) |
| 19. Asymmetric VE responsive to all flow components with a time lag error of 0.125 s and irregular waves, steady horizontal current | $\Delta C(t) = 4.0\tanh[0.1\lvert U(t-0.125)\rvert]$; $u \geq 0$<br>$\Delta C(t) = 0.7\tanh[0.07\lvert U(t-0.125)\rvert]$; $u < 0$ | ~4 | Irregular intermediate water waves based on LWF E11 near-bottom pressure time series (see text) | +5 | −98 (−40 if current direction shifted 180°) |
| 20. Symmetric VE responsive to all flow components with a time lag error of 0.125 s and irregular waves, steady horizontal current | $\Delta C(t) = (0.8)\tanh[0.3\lvert U(t-0.125)\rvert]$ | ~8 | Irregular deep-water waves (mean depth = 47 m) based on Oregon shelf near-bottom pressure time series (see text) | +4 | 0.1 |

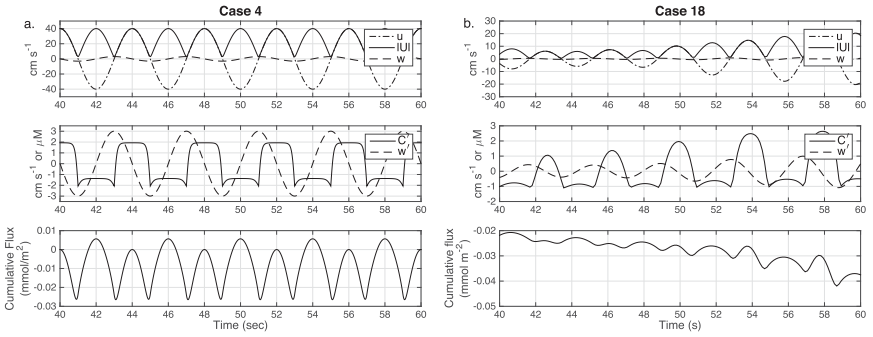


FIG. 9. Illustrations of model cases 4 and 18 from Table 3. For each case $C'$ is created by the VE model. The cumulative flux $= \sum_0^t w'C'$.

the relative asymmetry and absolute amplitudes of the velocity responses do affect the model fluxes (case 11 vs 13 and 14). Case 17 shows that if wave-driven variations in $w$ are reduced relative to $u$, as occurs at smaller distances above the bed, then velocity effect biases will decrease (Table 3).

As final model scenarios, ideal wave velocities that mimic the irregular waves during LWF E11 were used in cases 18 and 19, and model wave velocities based on observations from the Oregon shelf (and discussed in the next section) were used in case 20. After band-passing the near-bottom pressure records from 30-min data records to isolate wave frequencies, near-bottom wave velocities were predicted from the pressure series and linear wave theory for these cases. Assuming inexact time series alignments of $\pm 0.125$ s, the irregular wave cycles seen in the flume translate into irregular accumulations in the false flux (Fig. 9b illustrates case 18). However, in cases 18 and 19, the predicted false flux magnitude is less than seen from the C1 measurements in Fig. 6d. This suggests either a more substantial time lag error was present in the data series producing Fig. 6d or that velocity effects stemming from and/or combining with turbulent motions may also contribute to artificial fluxes under waves (Holtappels et al. 2015). Furthermore, as shown above, microelectrode velocity effects and associated response lags appear to be variable within even brief time series. The cumulative cospectra in Fig. 6d stem from the application of fixed lag corrections to all time points from two sensors over a 30-min record. Conceptually, lags can be envisioned as dependent on 1) the instantaneous water velocity [speed and direction, which alter the boundary layer thickness at the tip; see also the discussion in Holtappels et al. (2015), as well as whether water parcels reach the microelectrode before or after the ADV sampling volume] and 2) sensor tip characteristics, such as membrane thickness that could also experience small changes due to pressure variations, abrasion, or fouling.

### e. *Sensor effects under field conditions with waves*

Confronted with major velocity effects in the microelectrode records from the LWF experiments, we were prompted to look for similar artifacts in field data collected with the same equipment. To this end we focused on a 12-h dataset collected on the Oregon shelf during a period with moderately large surface waves and variable mean velocities (Fig. 10). Although two microelectrodes were utilized during the deployment, only one held a constant calibration. The construction properties of this sensor are given in Table 2 and were much like the sensors used in the LWF. Mean microelectrode concentrations, recorded for 30-min data segments (24.5 cm above the bottom), are shown in Fig. 10b relative to the record from optode 1 (positioned 21 cm above the bottom on the BOXER leg). Figure 10b also depicts the concentration difference measured by optode 2 (47 cm above the bottom) and optode 1 to illustrate periods when the bottom boundary layer vertical oxygen gradient was changing due to unsteady source or sink terms likely linked to advection.

Derived EC fluxes (Fig. 10c) were calculated both with and without shifting the oxygen time series for a typical sensor response time lag equaling 0.5 s. This time lag was suggested by cross-correlation analyses between $C'$ and $u$ in several selected 2-min data segments with strong wave signals, but we also found that no maximum (or minimum) cross-correlation index corresponding to lags $\leq 2$ s resulted for much of the deployment using $C'$ and any velocity parameter (e.g., $u$, $u'$, $w'$, $|U|$).

The derived fluxes equate to $-4.1 \pm 1.8$ (SE, $n = 22$) mmol m$^{-2}$ day$^{-1}$ using the lag-corrected oxygen series or $-5.2 \pm 1.8$ (SE, $n = 22$) mmol m$^{-2}$ day$^{-1}$ with no lag correction. These fluxes are smaller than average shelf-depth seafloor oxygen consumption rates (Glud 2008) but similar to benthic chamber derivations from a number of sites in deeper water on the Oregon shelf (Fuchsman et al. 2015). One 30-min burst near the 9-h

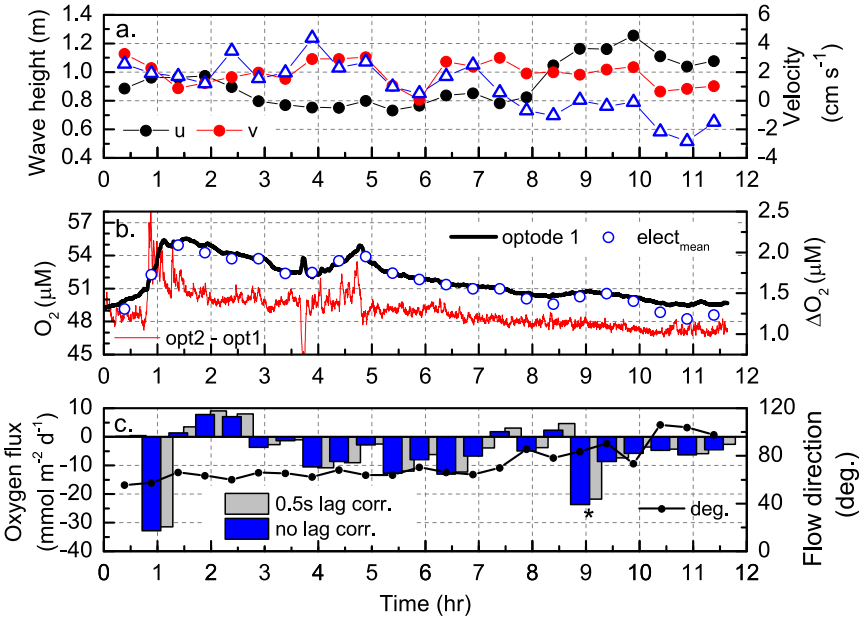


FIG. 10. Results from a 12-h BOXER deployment on the Oregon shelf at 48-m depth showing (a) 30-min averages of horizontal velocity components before rotation and $H_s$ (blue triangles), (b) dissolved oxygen measured by optode and as 30-min microelectrode averages, and (c) 30-min vertical eddy $O_2$ fluxes. The first 500 s of the EC data were excluded to allow for sensor equilibration. In (b) the difference in concentrations measured by vertically separated optodes is also portrayed. The starred 30-min flux in (c) had an abrupt microelectrode change, making it in error.

mark displayed a drop in the microelectrode signal over about 3 min followed by an abrupt return to prior levels, suggesting something had stuck to the sensor tip. Because of this clear artifact, the flux from this interval was omitted from the computed means for the deployment and from further analyses. At other times, fluxes appear to respond to transient advective forcing (Holtappels et al. 2013) or water column "storage" (Rheuban et al. 2014), meaning that, for example, when $dC/dt$ is trending sharply positive (near the 1-h mark), greater negative fluxes are induced, or when the current direction and intensity shifts (near the 8-h mark), fluxes fluctuate between positive and negative. Any velocity effect in the microelectrode measurements that could bias the fluxes cannot be ascertained by this level of analysis, except to note that unlike in the LWF, the fluxes were not very sensitive to shifting the oxygen time series (even by as much as 2 s).

To examine these field measurements more closely, we first took several 2-min data segments when the waves were pronounced and prepared plots of $C$ versus directional resultant velocities (three examples are given in Fig. 11) to look for velocity dependences within the oxygen measurements. Most of these plots (as well as the time series themselves) did suggest an oxygen signal modulated by waves that could arise from a velocity effect. Although some directional dependence (asymmetry) appears present, a simple overall nondirectional model approximation of the apparent velocity effect was derived [after Eq. (3)] because the flow direction with respect to the sensor's orientation changed throughout the deployment:

$$\Delta C_{\mathrm{VE}}(t) = (0.8)\tanh[0.3|U(t)|]. \qquad (4)$$

The model parameters from Eq. (4) and the bottom water concentration imply the stirring sensitivity for sensor 297 (Table 2) was ~1.65%, which we then used to estimate other parameters in the velocity effect model presented in Holtappels et al. (2015) (Fig. 11a). This stirring sensitivity is consistent in magnitude with other microelectrodes, as shown previously, but it also could be overestimated if some of the observed variability was generated by a wave-pumped oxygen gradient in the bottom water column. In addition, even in 2-min segments there is a great deal of data scatter around the model. Very likely this scatter stems from other drivers of $O_2$ signal variability besides flow speed and direction.

Next, we examined within 30-min intervals whether high (0.35–4 Hz), medium (capturing most shelf-depth surface waves: 0.06–0.35 Hz), or low (<0.06 Hz) frequency ranges dominated cumulative fluxes and if the

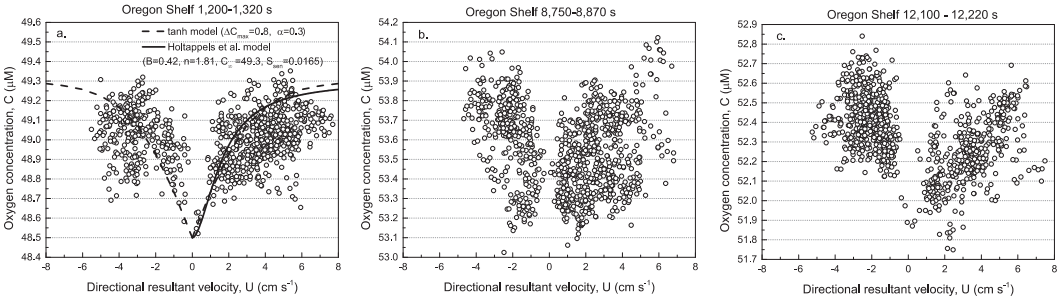


FIG. 11. (a)–(c) Measured oxygen concentration vs directional resultant velocity from three 2-min examples of EC measurements made in July 2013 at the Oregon shelf field site. In (a) VE models are superimposed with derived parameters that reflect the displayed units of the axes. Oxygen series based on these models did not yield EC fluxes comparable to the measurements (see text).

sign of the flux was consistent across ranges. Our reasoning was that velocity effects tied to waves would be seen at the medium frequencies, and they should produce a bias with a consistent sign in all bursts with a fixed response time lag adjustment (set to 0.5 s) and similar flow direction.

Somewhat unexpectedly, the results of these analyses show that the EC fluxes derived from our Oregon shelf example arise in large part from true low-frequency variations (Table 4). Low-frequency changes in oxygen are inferred to be real because they are also captured in the optode records. Individual linearly detrended 30-min time series show changes in oxygen on >20-s time scales that we attribute to slow, large-scale eddies or transient advective mixing. However, oxygen changes at wave frequencies yielded EC fluxes generally opposite in sign to the low-frequency fluxes until the dominant direction of flow shifted ~30° in the final hours of the deployment. The overall effect was to reduce the derived oxygen uptake rate by 2.7 mmol $m^{-2}$ $day^{-1}$ (the average flux in the wave frequency band). This magnitude of change cannot be easily recreated from velocity effects and a final field mimicking wave model case (as shown by case 20 in Table 3) primarily because model $w'$ oscillations derived at the observed water depth are very small and our model omits turbulence. However, larger $w'$ variations due to turbulence or advection combined with $C'$ oscillations created by the still significant horizontal wave velocity variations remain a mechanism for generating velocity effect biases within the cumulative fluxes from middle frequencies (Table 4).

Two approaches to estimate artificial fluxes generated from velocity effects in the presence of turbulence have been proposed by Holtappels et al. (2015). The first is based on creating an artificial oxygen time series from the sensor's velocity effect model and the observed velocity time series, dampening the fluctuations to account for possible response time attenuation, and deriving the artificial flux using the same data treatments applied to measurements. Although we found similar correction methods did not work well with the flume data, we attempted these calculations with the field measurements and the velocity effect parameters given in Eq. (4). The resultant artificial flux estimate for the full deployment was −7.4 ± 1.4 (SE, $n$ = 22) mmol $m^{-2}$ $day^{-1}$, which if subtracted from the measured flux yields a new in situ estimate (+3.3) that is positive and so not likely representative of the site's benthic $O_2$ flux. Furthermore, the measured fluxes derived from individual 30-min data segments are not significantly correlated with the artificial fluxes derived for the same segments ($r$ = 0.21, $n$ = 22). Based on these outcomes, we conclude that this approach exaggerates predictions of velocity effect bias. In this instance the overestimate could be because the microelectrode's velocity effect transfer function was not precisely known, and/or because variable flow conditions necessitate a velocity effect model that changes over the course of the deployment.

The second model proposed by Holtappels et al. (2015) to predict a false EC flux is based on Reynolds stress assessments and a sensor velocity effect transfer factor $F$ calculated from the first derivative of the velocity effect relationship between $C$ and velocity. By this model $\mathrm{ECflux_{art}} = F\overline{w'u'}$ [Holtappels et al. 2015, Eq. (5)]; however, the authors caution that 1) the model requires the microelectrode tip is pointed consistently into the flow and 2) it neglects response time concerns). In the Oregon field case, we have estimated $F$ = 18.8 μM s $m^{-1}$ (using velocity effect parameters from Fig. 11a). Combining this estimate of $F$ with the range of Reynolds stresses reported in Table 4 yields artificial fluxes equaling −16.2 ± 9.7 mmol $m^{-2}$ $day^{-1}$ (SE, $n$ = 23). As these model predictions are much greater in magnitude than the fluxes derived from the overall measurements or the first model, it seems this model further exaggerates artificial flux contributions.

TABLE 4. Further analyses of 30-min time series from the Oregon shelf deployment. Before assessing EC fluxes, the entire oxygen time series was shifted for a 0.5-s response lag.

| Measurement interval (hours after start of deployment) | $H_s$ (m) | $T_p$ (s) | Angle of dominant flow* (°) | Total EC flux (4 → 0.0005 Hz), (mmol m$^{-2}$ day$^{-1}$) | Cumulative EC flux (4 → 0.35 Hz) (mmol m$^{-2}$ day$^{-1}$) | Cumulative EC flux (0.35 → 0.06 Hz) (mmol m$^{-2}$ day$^{-1}$) | Cumulative EC flux (0.06 → 0.0005 Hz) (mmol m$^{-2}$ day$^{-1}$) | Reynolds stress $\overline{w'u'}$ (m$^2$ s$^{-2}$) |
|---|---|---|---|---|---|---|---|---|
| 0.14–0.64 | 1.1 | 7.9 | 55.7 | 0.4 | −0.1 | 3.0 | −2.6 | $-1.2 \times 10^{-5}$ |
| 0.64–1.14 | 1.0 | 7.9 | 57.4 | −31.5 | −0.5 | 5.9 | −36.9 | $-1.3 \times 10^{-5}$ |
| 1.14–1.64 | 1.0 | 7.9 | 66.1 | 3.5 | 0.3 | 7.0 | −3.8 | $-7.8 \times 10^{-6}$ |
| 1.64–2.14 | 0.9 | 7.9 | 63.5 | 9.1 | 0.1 | 5.6 | 3.4 | $-7.1 \times 10^{-6}$ |
| 2.14–2.64 | 1.1 | 8.1 | 60.2 | 8.0 | 0.2 | 7.4 | 0.4 | $-1.1 \times 10^{-5}$ |
| 2.64–3.14 | 1.0 | 8.3 | 66.0 | −2.7 | 0.1 | 4.6 | −7.3 | $-4.1 \times 10^{-6}$ |
| 3.14–3.64 | 1.0 | 8.1 | 65.5 | −1.0 | 0.0 | 2.5 | −3.5 | $-5.0 \times 10^{-6}$ |
| 3.64–4.14 | 1.2 | 7.9 | 62.5 | −10.8 | 0.1 | 0.4 | −11.3 | $-2.5 \times 10^{-5}$ |
| 4.14–4.64 | 1.0 | 7.9 | 68.3 | −9.0 | −0.2 | 2.8 | −11.6 | $-9.9 \times 10^{-6}$ |
| 4.64–5.14 | 1.1 | 8.1 | 63.8 | −2.5 | 0.2 | 3.5 | −6.2 | $-6.2 \times 10^{-6}$ |
| 5.14–5.64 | 0.9 | 8.3 | 64.0 | −12.1 | 0.1 | 1.2 | −13.4 | $-9.8 \times 10^{-6}$ |
| 5.64–6.14 | 0.9 | 8.1 | 70.5 | −6.2 | 0.2 | 3.0 | −9.4 | $-3.5 \times 10^{-6}$ |
| 6.14–6.64 | 1.0 | 7.9 | 66.3 | −12.3 | −0.1 | 1.9 | −14.1 | $-1.6 \times 10^{-5}$ |
| 6.64–7.14 | 1.1 | 8.1 | 64.3 | −3.9 | 0.2 | 3.6 | −7.8 | $-1.1 \times 10^{-5}$ |
| 7.14–7.64 | 0.9 | 7.9 | 70.0 | 3.1 | −0.2 | 6.5 | −3.1 | $-6.1 \times 10^{-6}$ |
| 7.64–8.14 | 0.7 | 8.1 | 85.6 | −3.8 | 0.0 | 4.0 | −7.8 | $-1.8 \times 10^{-5}$ |
| 8.14–8.64 | 0.7 | 8.3 | 78.3 | 4.7 | −0.3 | 4.4 | 0.7 | $-1.2 \times 10^{-5}$ |
| 8.64–9.14 | 0.8 | 7.9 | 83.5 | — | — | — | — | $-1.4 \times 10^{-5}$ |
| 9.14–9.64 | 0.8 | 8.1 | 90.5 | −7.4 | −0.3 | −3.5 | −3.6 | $-1.2 \times 10^{-5}$ |
| 9.64–10.14 | 0.8 | 7.9 | 73.6 | −3.6 | −0.4 | 1.4 | −4.6 | $-2.0 \times 10^{-5}$ |
| 10.14–10.64 | 0.6 | 7.9 | 106.2 | −4.3 | −0.5 | −0.8 | −3.1 | $-3.3 \times 10^{-6}$ |
| 10.64–11.14 | 0.5 | 8.1 | 103.8 | −5.9 | −0.1 | −2.3 | −3.5 | $-1.9 \times 10^{-6}$ |
| 11.14–11.67 | 0.6 | 7.8 | 97.5 | −2.7 | −0.7 | −2.3 | 0.3 | $-1.8 \times 10^{-6}$ |
| Mean ± SE | | | | −4.1 ± 1.8 | −0.1 ± 0.1 | 2.7 ± 0.6 | −6.8 ± 1.7 | $-1.0 \pm 0.6 \times 10^{-5}$ |

* The asterisk means it was measured from the Vector's $x$ axis and inferred from rotation methods. It is plotted in Fig. 10c.

A final approach to assess possible artificial fluxes in EC datasets from environments with waves might be to simply bandpass out wave peaks from spectral representations of the oxygen measurements or eddy fluxes. However, physical oceanographers concerned about "wave bias" caution that wave peaks occur at frequencies at which turbulence is also energetic and able to contribute to turbulent fluxes (Bricker and Monismith 2007). Here we have a similar but substantially more complicated problem in that 1) velocity measurements may carry wave bias that stems from small tilt errors not removed by rotation methods that are combined with vertical transport by waves (Shaw and Trowbridge 2001), 2) time lag biases may arise from wave-driven fluctuations in vertical velocity being out of sync with oxygen fluctuations created by advection of the vertical oxygen gradient (Berg et al. 2015), and 3) oxygen measurements may also reflect velocity effects out of alignment with velocities. Assessing flux contributions at wave frequencies (as in Table 4) does at least provide an estimate of the maximum probable wave and velocity effect bias in a dataset. To learn more in future studies, the EC method would be well served if further comparisons were made between systems with pairs of collocated microelectrodes and different types of oxygen sensors to identify what oxygen signals are coherent, and what variances are created from velocity effects.

## 5. Conclusions and recommendations

The results of the experiments presented here from an LWF and the Oregon shelf demonstrate that in the presence of high-energy waves, eddy covariance measurements must be carefully scrutinized to identify possible biases stemming from velocity effects and other sensor limitations. Time series measurements of velocity components in the LWF and their variability binned over four frequency ranges (Fig. 4) showed that under irregular waves and a water depth $< 3$ m, wave frequencies dominated vertical velocity variations 15 or 30 cm above the bed, and that high-frequency turbulence was not significantly enhanced beneath the frame of the BOXER tripod. In other words, it appears that wakes shed from frame parts generally dissipated before reaching or missed the measurement volume in the flow regimes generated. Similarly, Williams et al. (2003) report surprisingly small modifications to local turbulence by a 1.4 times wider and heavier tripod frame studied in an LWF in the Netherlands.

However, the five individual ADVs employed in this LWF study did not always record equal wave velocities. What was most puzzling was that the two Vectors appeared to underrepresent velocities during some but not all experiments. These occurrences were not related to the nominal velocity setting of the Vector, orientation, signal-to-noise ratios (SNR) (all beams $> 20$ db, considered the threshold for high quality by Nortek), or despiking (although despiking did reduce variability in all velocity records by different degrees). Expressions for predicting $u(x, z, t)$ from linear wave theory (e.g., Dean and Dalrymple 1992) at a height $z = 15$ or 30 cm cannot produce std($u'$) values that are reduced by 30% (as in Fig. 4) using variables of water depth and wave height expected at different locations within the flume. Therefore, we are concerned that the Vector ADV can underevaluate true flow characteristics under energetic waves. A contributing factor may be the presence of the microelectrode(s) at the edge of the sampling volume. If small misalignments caused the tips to protrude into the ADV's sampling space during some experiments, then acoustic returns from these nonmoving objects could bias (low) the ADV's phase data that are then converted into speed (Voulgaris and Trowbridge 1998).

Our LWF studies also revealed the potential for EC biases in the presence of waves due to microelectrode velocity effects in combination with time series alignment errors arising from the oxygen sensor's longer response time compared to the ADV. A response time lag adjustment error will alter the phase relationship between $w'$ and $C'$, sometimes with extreme consequences for flux derivations (Berg et al. 2015). When an oxygen sensor has in addition a velocity response to progressive wave motions (driven largely by $u'$ and out of phase with $w'$), these effects will add to the creation of a false flux (as illustrated by simple model cases combining waves and currents and/or displaying velocity effects that change with flow direction; Table 3). Perfect time series alignment is difficult to achieve when both flow speed and direction are oscillating.

Microelectrodes with shorter response times tend to have thinner membranes and greater velocity sensitivities. The sensors used in this study exhibited maximum velocity sensitivities of up to 1.65%, and they showed a directional dependence such that the velocity effect was greater when the sensor was pointed into the flow (Fig. 6). The likely cause is greater boundary layer compression at the sensor tip when strong flow is directed at the sensor. We have confirmed this directional difference with additional sensors in other experiments using a small recirculating flume, and using a wave tank to produce standing waves (see Berg et al. 2016).

The dramatic impacts of microelectrode velocity effects in combination with sensor response time on extracted eddy fluxes from the LWF data led us to examine EC measurements in a field case from the Oregon shelf. What distinguished the field case from the flume

was: deeper water (~48 m), longer period waves (~8 s), a lower background $O_2$ concentration (49–55 $\mu$M), and mean flows that changed direction over time. The total EC fluxes derived ($-4.1 \pm 1.8$ mmol m$^{-2}$ day$^{-1}$ (SE, $n = 22$)] equate to reasonable benthic oxygen consumption rates for this environment when compared to benthic chamber fluxes (Fuchsman et al. 2015). However, these rates were reduced by possible biases or real flux contributions at wave frequencies that averaged $+2.7 \pm 0.6$ mmol m$^{-2}$ day$^{-1}$ (Table 4). A key factor that may have helped reduce velocity bias in fluxes from the Oregon shelf as compared to flume observations is that vertical wave velocity components become small in deeper water as was illustrated by our wave model (case 20). Also, when the bottom water $O_2$ concentration is low, the magnitude of any velocity effect signal ($\Delta C_{VE}$) will be reduced because it scales with the concentration external to the tip.

The construction of oxygen microelectrodes according to the established approach of Revsbech (1989) makes it nearly impossible to eliminate velocity effects while preserving a rapid response ($t_{90} \leq 0.5$ s). The sensors used in this study were carefully characterized and of high quality, but they still produced biases that were exacerbated by the extreme variability of short-period energetic wave motions. In such situations, in future studies we recommend using sensors with the smallest feasible tip inner and outer diameters (<2 $\mu$m), thicker membranes (~10 $\mu$m), and recessed cathodes (~5–10 $\mu$m) to minimize velocity effects. Such microelectrodes will have relatively lower sensitivities and slower responses, but these factors can be controlled for with high-quality amplifiers and better corrections for response time delays (Berg et al. 2015; Donis et al. 2015). Other sensor technologies, such as optodes, are not completely free of the effects of sensor boundary layer dynamics (Bittig et al. 2014), but they may prove less problematic for experiments under waves (Chipman et al. 2012; Holtappels et al. 2015). Approaches that may control the $O_2$ sensor's boundary layer thickness and shorten sensor response times are ultimately what are needed.

*Acknowledgments.* This research was supported under NSF Grant OCE-1061218 to CER and HTO, and OCE-1061364 and OCE-1334848 to PB. We thank T. Maddux, R. D. Sanders and C. Doolan for their assistance during the wave flume experiments; K. McCann-Grosvenor for construction and characterization of the oxygen microelectrodes; and the officers and crew of the R/V *Oceanus* for assistance in executing the field deployment on the Oregon shelf. Two reviews from M. Holtappels provided insights that helped improve the manuscript greatly. D. McGinnis and one anonymous reviewer also provided helpful reviews.

## REFERENCES

Berg, P., and M. Huettel, 2008: Monitoring the seafloor using the noninvasive eddy correlation technique: Integrated benthic exchange dynamics. *Oceanography*, **21** (4), 164–167, doi:10.5670/oceanog.2008.13.

——, H. Røy, F. Janssen, V. Meyer, B. B. Jørgensen, M. Huettel, and D. de Beer, 2003: Oxygen uptake by aquatic sediments measured with a novel non-invasive eddy-correlation technique. *Mar. Ecol. Prog. Ser.*, **261**, 75–83, doi:10.3354/meps261075.

——, R. N. Glud, A. Hume, H. Stahl, K. Oguri, V. Meyer, and H. Kitazato, 2009: Eddy correlation measurements of oxygen uptake in deep ocean sediments. *Limnol. Oceanogr. Methods*, **7**, 576–584, doi:10.4319/lom.2009.7.576.

——, and Coauthors, 2013: Eddy correlation measurements of oxygen fluxes in permeable sediments exposed to varying current flow and light. *Limnol. Oceanogr.*, **58**, 1329–1343, doi:10.4319/lo.2013.58.4.1329.

——, C. E. Reimers, J. H. Rosman, M. Huettel, M. L. Delgard, M. A. Reidenbach, and H. T. Özkan-Haller, 2015: Technical note: Time lag correction of aquatic eddy covariance data measured in presence of waves. *Biogeosciences*, **12**, 6721–6735, doi:10.5194/bg-12-6721-2015.

——, D. J. Koopmans, M. Huettel, H. Li, K. Mori, and A. Wüest, 2016: A new robust oxygen-temperature sensor for aquatic eddy covariance measurements. *Limnol. Oceanogr. Methods*, doi:10.1002/lom3.10071, in press.

Bittig, H. C., B. Fiedler, R. Scholz, G. Krahmann, and A. Körtzinger, 2014: Time response of oxygen optodes on profiling platforms and its dependence on flow speed and temperature. *Limnol. Oceanogr. Methods*, **12**, 617–636, doi:10.4319/lom.2014.12.617.

Boudreau, B. P., 1997: *Diagenetic Models and Their Implementation*. Springer-Verlag, 414 pp.

Bricker, J. D., and S. G. Monismith, 2007: Spectral wave–turbulence decomposition. *J. Atmos. Oceanic Technol.*, **24**, 1479–1487, doi:10.1175/JTECH2066.1.

Chipman, L., M. Huettel, P. Berg, V. Meyer, I. Klimant, R. Glud, and F. Wenzhoefer, 2012: Oxygen optodes as fast sensors for eddy correlation measurements in aquatic systems. *Limnol. Oceanogr. Methods*, **10**, 304–316, doi:10.4319/lom.2012.10.304.

Dean, R. G., and R. A. Dalrymple, 1992: *Water Wave Mechanics for Engineers and Scientists*. Advanced Series on Ocean Engineering, Vol. 2, World Scientific Publishing, 353 pp.

Doering, J. C., and A. J. Baryla, 2002: An investigation of the velocity field under regular and irregular waves over a sand beach. *Coastal Eng.*, **44**, 275–300, doi:10.1016/S0378-3839(01)00037-0.

Donis, D., and Coauthors, 2015: An assessment of the precision and confidence of aquatic eddy correlation measurements. *J. Atmos. Oceanic Technol.*, **32**, 642–655, doi:10.1175/JTECH-D-14-00089.1.

Fick, A., 1855: On liquid diffusion. *Philos. Mag. Ser. 4*, **10**, 30–39, doi:10.1080/14786445508641925.

Fuchsman, C. A., A. H. Devol, Z. Chase, C. E. Reimers, and B. Hales, 2015: Benthic fluxes on the Oregon shelf. *Estuarine Coastal Shelf Sci.*, **163**, 156–166, doi:10.1016/j.ecss.2015.06.001.

Glud, R. N., 2008: Oxygen dynamics of marine sediments. *Mar. Biol. Res.*, **4**, 243–289, doi:10.1080/17451000801888726.

——, J. K. Gundersen, and N. B. Ramsing, 2000: Electrochemical and optical oxygen microsensors for in situ measurements. *In Situ Monitoring of Aquatic Systems: Chemical Analysis and Speciation*, J. Buffle and G. Horvai, Eds., IUPAC Series on Analytical and Physical Chemistry of Environmental Systems, Vol. 6, John Wiley and Sons Ltd., 19–73.

Goring, D. G., and V. I. Nikora, 2002: Despiking acoustic Doppler velocimeter data. *J. Hydraul. Eng.*, **128**, 117–126, doi:10.1061/(ASCE)0733-9429(2002)128:1(117).

Grant, W. D., and O. S. Madsen, 1986: The continental shelf bottom boundary layer. *Annu. Rev. Fluid Mech.*, **18**, 265–305, doi:10.1146/annurev.fl.18.010186.001405.

Gundersen, J. K., N. B. Ramsing, and R. N. Glud, 1998: Predicting the signal of $O_2$ microsensors from physical dimensions, temperature, salinity and $O_2$ concentration. *Limnol. Oceanogr.*, **43**, 1932–1937, doi:10.4319/lo.1998.43.8.1932.

Gust, G., K. Booij, W. Helder, and B. Sundby, 1987: On the velocity sensitivity (stirring effect) of polarographic oxygen microelectrodes. *Neth. J. Sea Res.*, **21**, 255–263, doi:10.1016/0077-7579(87)90001-9.

Holtappels, M., R. N. Glud, D. Donis, B. Liu, A. Hume, F. Wenzhöfer, and M. M. M. Kuypers, 2013: Effects of transient bottom water currents and oxygen concentrations on benthic exchange rates as assessed by eddy correlation measurements. *J. Geophys. Res. Oceans*, **118**, 1157–1169, doi:10.1002/jgrc.20112.

——, C. Noss, K. Hancke, C. Cathalot, D. F. McGinnis, A. Lorke, and R. N. Glud, 2015: Aquatic eddy correlation: Quantifying the artificial flux caused by stirring-sensitive $O_2$ sensors. *PLoS One*, **10**, e0116564, doi:10.1371/journal.pone.0116564.

Huettel, M., and I. T. Webster, 2001: Porewater flow in permeable sediments. *The Benthic Boundary Layer: Transport Processes and Biogeochemistry*, B. P. Boudreau and B. B. Jørgensen, Eds., Oxford University Press, 144–177.

Jahnke, R., M. Richards, J. Nelson, C. Robertson, A. Rao, and D. Jahnke, 2005: Organic matter remineralization and porewater exchange rates in permeable South Atlantic Bight continental shelf sediments. *Cont. Shelf Res.*, **25**, 1433–1452, doi:10.1016/j.csr.2005.04.002.

Kuwae, T., K. Kamio, T. Inoue, E. Miyoshi, and Y. Uchiyama, 2006: Oxygen exchange flux between sediment and water in an intertidal sandflat, measured *in situ* by the eddy-correlation method. *Mar. Ecol. Prog. Ser.*, **307**, 59–68, doi:10.3354/meps307059.

Lorrai, C., D. F. McGinnis, P. Berg, A. Brand, and A. Wüest, 2010: Application of oxygen eddy correlation in aquatic systems. *J. Atmos. Oceanic Technol.*, **27**, 1533–1546, doi:10.1175/2010JTECHO723.1.

McCann-Grosvenor, K., C. E. Reimers, and R. D. Sanders, 2014: Dynamics of the benthic boundary layer and seafloor contributions to oxygen depletion on the Oregon inner shelf. *Cont. Shelf Res.*, **84**, 93–106, doi:10.1016/j.csr.2014.05.010.

McGinnis, D. F., S. Sommer, A. Lorke, R. N. Glud, and P. Linke, 2014: Quantifying tidally-driven benthic oxygen exchange across permeable sediments: An aquatic eddy correlation study. *J. Geophys. Res. Oceans*, **119**, 6918–6932, doi:10.1002/2014JC010303.

Reimers, C. E., H. A. Stecher, G. L. Taghon, C. M. Fuller, M. Huettel, A. Rusch, N. Ryckelynck, and C. Wild, 2004: In situ measurements of advective solute transport in permeable shelf sands. *Cont. Shelf Res.*, **24**, 183–201, doi:10.1016/j.csr.2003.10.005.

——, H. T. Özkan-Haller, P. Berg, A. Devol, K. McCann-Grosvenor, and R. D. Sanders, 2012: Benthic oxygen consumption rates during hypoxic conditions on the Oregon continental shelf: Evaluation of the eddy correlation method. *J. Geophys. Res.*, **117**, C02021, doi:10.1029/2011JC007564.

Revsbech, N. P., 1989: An oxygen microsensor with a guard cathode. *Limnol. Oceanogr.*, **34**, 474–478, doi:10.4319/lo.1989.34.2.0474.

Rheuban, J. E., P. Berg, and K. J. McGlathery, 2014: Multiple timescale processes drive ecosystem metabolism in eelgrass (*Zostera marina*) meadows. *Mar. Ecol. Prog. Ser.*, **507**, 1–13, doi:10.3354/meps10843.

Rusch, A., M. Huettel, C. E. Reimers, G. L. Taghon, and C. M. Fuller, 2003: Activity and distribution of bacterial populations in Middle Atlantic Bight shelf sands. *FEMS Microbiol. Ecol.*, **44**, 89–100, doi:10.1111/j.1574-6941.2003.tb01093.x.

Shaw, W. J., and J. H. Trowbridge, 2001: The direct estimation of near-bottom turbulent fluxes in the presence of energetic wave motions. *J. Atmos. Oceanic Technol.*, **18**, 1540–1557, doi:10.1175/1520-0426(2001)018<1540:TDEONB>2.0.CO;2.

Voulgaris, G., and J. H. Trowbridge, 1998: Evaluation of the acoustic Doppler velocimeter (ADV) for turbulence measurements. *J. Atmos. Oceanic Technol.*, **15**, 272–288, doi:10.1175/1520-0426(1998)015<0272:EOTADV>2.0.CO;2.

Williams, J. J., P. S. Bell, L. E. Coates, N. Metje, and R. Selwyn, 2003: Interactions between a benthic tripod and waves on a sandy bed. *Cont. Shelf Res.*, **23**, 355–375, doi:10.1016/S0278-4343(02)00188-7.